INVITED PAPER

# Simultaneous Molecular and Hypoxia Imaging of Brain Tumors *In Vivo* Using Spectroscopic Photoacoustic Tomography

*This noninvasive imaging technology, with high resolution and strong contrast, promises to open better understanding of the development of brain tumors and their treatment.*

By Meng-Lin Li, *Member IEEE*, Jung-Taek Oh, Xueyi Xie, Geng Ku, Wei Wang, Chun Li, Gina Lungu, George Stoica, and Lihong V. Wang, *Fellow IEEE*

**ABSTRACT** | Noninvasive molecular and functional imaging *in vivo* is promising for detecting and monitoring various physiological conditions in animals and ultimately humans. To this end, we present a novel noninvasive technology, spectroscopic photoacoustic tomography (SPAT), which offers both strong optical absorption contrast and high ultrasonic spatial resolution. Optical contrast allows spectroscopic separation of signal contributions from multiple optical absorbers (e.g., oxyhemoglobin, deoxyhemoglobin, and a molecular contrast agent), thus enabling simultaneous molecular and functional imaging. SPAT successfully imaged with high resolution the distribution of a molecular contrast agent targeting integrin $\alpha_v\beta_3$ overexpressed in human U87 glioblastomas in nude mouse brains. Simultaneously, SPAT also imaged the hemoglobin oxygen saturation and the total hemoglobin concentration of the vasculature, which revealed hypoxia in tumor neovasculature. Therefore, SPAT can potentially lead to better understanding of the interrelationships between hemodynamics and specific biomarkers associated with tumor progression.

**KEYWORDS** | Functional imaging; hemoglobin oxygen saturation; molecular imaging; spectroscopic photoacoustic tomography; total hemoglobin concentration

## I. INTRODUCTION

Molecular imaging offers an extraordinary opportunity for studying diseases at the molecular level noninvasively and quantitatively [1]–[4]. With the marriage of state-of-the-art noninvasive imaging technologies with molecular- and cell-biology techniques, the advances emerging from molecular imaging will enhance our understanding of disease pathophysiology and lead to better methods for studying biological processes as well as diagnosing and managing diseases. For example, molecular imaging offers a more specific approach to the earlier detection and characterization of tumor biology and angiogenesis because it targets imaging probes at specific molecular markers expressed on the neoendothelial- and tumor-cell surface. Such techniques will accelerate the development of novel molecular-targeted anticancer therapeutics [5]–[8].

Manuscript received June 1, 2007; revised September 5, 2007. This work was supported in part by the National Institutes of Health under Grants R01 EB000712 and R01 NS46214.

**M.-L. Li** is with the Department of Electrical Engineering, National Tsing Hua University, Hsinchu 30013, Taiwan, R.O.C.

**J.-T. Oh** and **X. Xie** are with the Optical Imaging Laboratory, Department of Biomedical Engineering, Texas A&M University, College Station, TX 77843-3120 USA.

**G. Ku** and **L. V. Wang** are with the Optical Imaging Laboratory, Department of Biomedical Engineering, Washington University in St. Louis, St. Louis, MO 63130-4899 USA (e-mail: lhwang@biomed.wustl.edu).

**W. Wang** and **C. Li** are with the Department of Experimental Diagnostic Imaging, University of Texas M. D. Anderson Cancer Center, Houston, TX 77030 USA.

**G. Lungu** and **G. Stoica** are with the Department of Veterinary Pathobiology, Texas A&M University, College Station, TX 77843-5547 USA.

Digital Object Identifier: 10.1109/JPROC.2007.913515

Three common noninvasive molecular imaging domains have been developed more or less in parallel: magnetic resonance imaging (MRI) [9]–[11], nuclear imaging (positron emission tomography [12], [13] and single photon emission computed tomography [14]), and optical imaging (bioluminescence [15] and fluorescence imaging [16]–[19]); in addition, ultrasound is also being developed [20]. Excellent reviews of these technologies are available in the literature [1]–[4].

Optical imaging is highly attractive owing to its potential for simultaneous functional and molecular imaging because endogenous molecules and exogenous molecular contrast agents can be measured at the same time. By accessing endogenous oxyhemoglobin ($HbO_2$) and deoxyhemoglobin (HbR) [21], [22], optical imaging can offer *in vivo* noninvasive functional imaging of blood oxygen saturation ($SO_2$) and total hemoglobin concentration (HbT). Imaging of the oxygenation status of tumors, especially hypoxia, is receiving more and more attention in assessing tumor growth, malignant progression, metastasis, and resistance to various therapies—including radiotherapy and chemotherapy as well as photodynamic therapy [23]–[27]. By accessing exogenous molecular contrast agents, optical imaging can offer *in vivo* noninvasive molecular imaging. Pure optical imaging, however, faces a major obstacle—the overwhelming optical scattering in biological tissue. As a result, its spatial resolution significantly decreases with increasing imaging depth, and it cannot image beyond the intact scalp and cranium of a small-animal head with high resolution.

Here, we present a novel molecular and functional imaging technique—spectroscopic photoacoustic tomography (SPAT)—for the detection and characterization of intracranial tumor xenografts in small animals *in vivo*. Photoacoustic tomography overcomes the resolution drawback of pure optical imaging while retaining the most compelling features of both optics and ultrasound—namely, high optical absorption contrast and submillimeter ultrasound resolution—up to an imaging depth of centimeters [28]–[32]. By changing the laser wavelength, SPAT can probe the optical absorption spectrum of an object. The measured spectrum can then be used to decode the contributions from three dominating optical absorbers—HbR, $HbO_2$, and an exogenous contrast agent—based on the differences in their molar optical extinction spectra. In this paper, the exogenous contrast agent is an indocyanine-green (ICG) derivative named IRDye800-NHS (Li-Cor, Inc.) conjugated with cyclic peptide cyclo(Lys-Arg-Gly-Asp-Phe) [c(KRGDf) for short] that targets integrin $\alpha_v\beta_3$; hereafter, it is referred to as IRDye800-c(KRGDf) [18]. IRDye800 provides both absorption and fluorescence primarily in the near-infrared (NIR) spectral region; the former effects a contrast in SPAT and the latter effects a contrast in fluorescence imaging. Therefore, SPAT not only can image the level of the contrast-agent uptake in the brain tumor xenograft, which is related to the hypermetabolism and angiogenesis of the tumor, but also can simultaneously image the $SO_2$ and the HbT in the tumor; in addition, conventional fluorescence imaging can corroborate the contrast-agent uptake with low spatial resolution.

Subsequent sections will show the following.

1) SPAT can image with high spatial resolution the distribution of the molecular contrast agent that targets a brain U87 glioblastoma tumor—which expresses integrin $\alpha_v\beta_3$—in a nude mouse through intact scalp and skull.
2) SPAT can image simultaneously functional parameters $SO_2$ and HbT in the brain tumor vasculature without any invasive biological modification such as opening a cranial window [33].
3) The complementary information from the functional and the molecular imaging can potentially prove to be useful for tumor diagnosis, prognosis, and cell-centered therapeutics.

## II. MATERIALS AND METHODS

### A. Tumor Cells and Animals

Human U87 glioblastoma tumor cells were implanted stereotactically into young adult immunocompromised nude mice (Harlan, Co.). The cell line was maintained in Dulbecco's Modified Eagle Medium (DMEM) culture medium with 10 000 units/ml penicillin and 10% fetal bovine serum (Gibco, Inc.). The implantation was performed on nude mice weighing about 20 grams under full anesthesia using a mixture of 87 mg/kg ketamine (Ketaset, Forth Dodge Animal Health) and 13 mg/kg xylazine (AnaSed, Lloyd Laboratories). One million cells were inoculated intracranially into the caudate nucleus at a 3 mm depth from the scalp surface with a volume of 7 $\mu$l [34].

One week post inoculation, 20 nmol of IRDye800-c(KRGDf) (University of Texas M. D. Anderson Cancer Center) [18] was systematically administered through the tail vein with mannitol, which permealized the blood brain barrier. Imaging was conducted $\sim$20 h after the injection of IRDye800-c(KRGDf). Throughout the SPAT experiment, the mouse was under full anesthesia and provided with oxygen; the body temperature of the nude mouse was maintained at 37° using a water heating pad; the pulse rate and arterial blood oxygenation were monitored using a pulse oximeter (Model 8600, Nonin Medical, Inc.) clamped on the back paw. After the experiment, the mouse was sacrificed; the mouse brain was harvested to make slides. The slides were divided into three interlaced groups. One group were imaged using the Odyssey fluorescence imaging system at 800 nm to verify the IRDye800-c(KRGDf) uptake. The other two groups were fixed; then, one group was stained with Thionine to

identify the tumor and the other group were stained with anti–von Willebrand factor VIII antibody to demonstrate the tumor-associated neovascularization.

All of the experimental animal procedures on nude mice were approved by the University Laboratory Animal Care Committee of Texas A&M University and were performed according to the guidelines of the U.S. National Institutes of Health [35].

### B. SPAT System for Noninvasive Imaging of Mouse Brain *In Vivo*

The experimental setup of *in vivo* SPAT of a nude mouse head is shown in Fig. 1. A tunable Ti:sapphire (Ti:Sa) nanosecond pulsed laser (LT-2211A, Lotis T II, Minsk, Belarus) pumped by an Nd:YAG laser (LS-2137/2, Lotis T II, Minsk) was employed to provide laser pulses with a pulse repetition frequency (PRF) of 10 Hz. The prism-directed laser beam was expanded by a concave lens, homogenized by a light diffuser, and then delivered to the animal head. The incident energy density of the laser beam on the surface of the mouse head was controlled at $\sim$20 mJ/cm$^2$ according to the ANSI standard [36]. The energy of each laser pulse was detected by a photodiode (PD) (DET110, ThorLabs, Inc.) and recorded by an oscilloscope (TDS5054, Tektronix, Inc.). The recorded PD signals were used to normalize the received PA signals; thus, the effect of laser energy fluctuation is compensated for. The nude mouse was restrained by a homemade mount and coated with a thin layer of ultrasonic coupling gel; then, its head protruded into the water tank through a hole in the bottom, where the hole was sealed with a piece of polyethylene membrane. Two ultrasonic transducers (V323/2.25 MHz and XMS-310/10 MHz, Panametrics) within the water tank detected the PA signals. The active areas of the 2.25- and 10-MHz transducers were 6 and 2 mm in diameter, respectively; the corresponding nominal bandwidths were 66% and 80%, respectively. A computer-controlled step motor rotated the two transducers through 120 positions along a complete circle to receive the PA signals at each position. These signals were low-pass filtered and amplified by ultrasonic receivers (5072PR, Panametrics). The amplified signals were then digitized and averaged 20 times at each scan position with a data acquisition card (CS14100, Gage, Inc.) operating at a 50-MHz sampling rate with 14-bit resolution. After a full circle is scanned, the digitized signals were used to reconstruct the distribution of the optical absorption in the imaging (x-y) plane with a modified back-projection algorithm [37].

Both the oscilloscope and the data acquisition card were synchronized by the Q-switch synchronization output from the pumping laser. The 2.25-MHz transducer was positioned at approximately the height of the tumor inoculation ($\sim$3 mm below the scalp surface) with a scanning radius of 4.5 cm to image the tumor. The 10-MHz transducer was located approximately at the height of the scalp surface with a scanning radius of 3.5 cm to image the brain cortex. Four laser wavelengths—764, 784, 804, and 824 nm—were used. The wavelength was automatically changed at each scanning position, instead of at the end of each circular scan, to reduce motion artifacts. In addition, the laser beam was blocked by a computer-controlled shutter during the translation of the transducer to reduce laser exposure of the tissue and laser bleaching of the contrast agent.

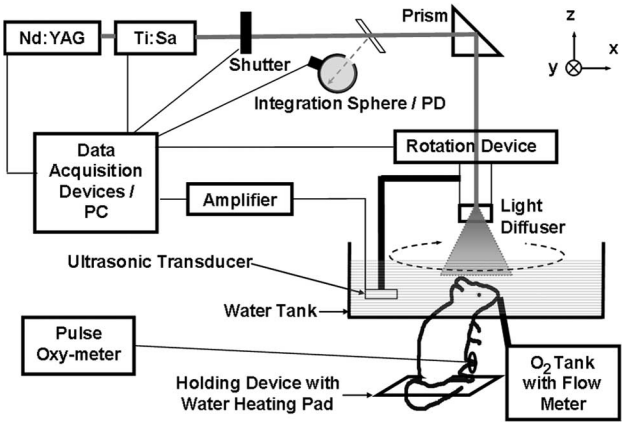


**Fig. 1.** *Experimental setup of SPAT for in vivo mouse brain imaging.*

### C. Principle of SPAT Imaging of HbR, $HbO_2$, and IRDye800-c(KRGDf)

SPAT separates the contributions from multiple absorbers based on the differences in their molar optical extinction spectra. Upon the administration of IRDye800-c(KRGDf), only three dominant absorbers [HbR, $HbO_2$, and IRDye800-c(KRGDf)] are imaged in the NIR spectral region. After being normalized by both the incident laser energy and the attenuation of the laser energy due to the skin and skull, the reconstructed PA image $A(\lambda_i, x, y)$ at the $i$th wavelength $\lambda_i$ can be expressed as

$$A(\lambda_i,x,y)=\varepsilon_{\mathrm{HbR}}(\lambda_i)C_{\mathrm{HbR}}(x,y)+\varepsilon_{\mathrm{HbO_2}}(\lambda_i)C_{\mathrm{HbO_2}}(x,y)+\varepsilon_{\mathrm{IRDye}}(\lambda_i)C_{\mathrm{IRDye}}(x,y) \quad (1)$$

apart from a constant factor. Here, $\varepsilon_{\mathrm{HbR}}(\lambda_i)$, $\varepsilon_{\mathrm{HbO_2}}(\lambda_i)$, and $\varepsilon_{\mathrm{IRDye}}(\lambda_i)$ are the known molar extinction coefficients (cm$^{-1}$M$^{-1}$) of HbR, $HbO_2$, and IRDye800-c(KRGDf) at wavelength $\lambda_i$, respectively (for the molar extinction spectra of the three absorbers, see Fig. 2). $C_{\mathrm{HbR}}(x,y)$, $C_{\mathrm{HbO_2}}(x,y)$, and $C_{\mathrm{IRDye}}(x,y)$ are the molar concentrations (M) of HbR, $HbO_2$, and IRDye800-c(KRGDf), respectively. Using multiwavelength measurements, $C_{\mathrm{HbR}}(x,y)$, $C_{\mathrm{HbO_2}}(x,y)$, and $C_{\mathrm{IRDye}}(x,y)$ can be estimated by solving the overdetermined set of linear equations, four equations

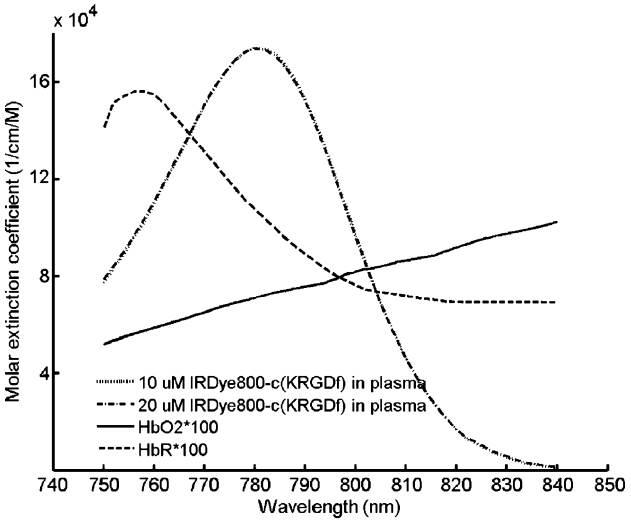


**Fig. 2.** *Molar extinction coefficient spectra of 10 $\mu$M IRDye800-c(KRGDf) in plasma, 20 $\mu$M IRDye800-c(KRGDf) in plasma, $HbO_2$, and HbR. Note that the values of $HbO_2$ and HbR are scaled up by two orders of magnitude for comparison with IRDye800-c(KRGDf). (For lists of values of $HbO_2$ and HbR, refer to http://www.omlc.ogi.edu/spectra/.)*

in this paper, represented by (1) using a standard linear least squares method

$$\begin{bmatrix} C_{\mathrm{HbR}}(x,y) \\ C_{\mathrm{HbO_2}}(x,y) \\ C_{\mathrm{IRDye}}(x,y) \end{bmatrix} = (\varepsilon^T\varepsilon)^{-1}\varepsilon^T\mathbf{A} \tag{2}$$

where $\mathbf{A} = \begin{bmatrix} A(\lambda_1,x,y) \\ A(\lambda_2,x,y) \\ \vdots \\ A(\lambda_N,x,y) \end{bmatrix}$ and

$$\varepsilon = \begin{bmatrix} \varepsilon_{\mathrm{HbR}}(\lambda_1) & \varepsilon_{\mathrm{HbO_2}}(\lambda_1) & \varepsilon_{\mathrm{IRDye}}(\lambda_1) \\ \varepsilon_{\mathrm{HbR}}(\lambda_2) & \varepsilon_{\mathrm{HbO_2}}(\lambda_2) & \varepsilon_{\mathrm{IRDye}}(\lambda_2) \\ & \vdots & \\ \varepsilon_{\mathrm{HbR}}(\lambda_N) & \varepsilon_{\mathrm{HbO_2}}(\lambda_N) & \varepsilon_{\mathrm{IRDye}}(\lambda_N) \end{bmatrix}.$$

With the estimated $C_{\mathrm{HbR}}(x,y)$ and $C_{\mathrm{HbO_2}}(x,y)$, the HbT and $SO_2$ images can be calculated point by point as follows [38]:

$$\mathrm{HbT}(x,y) = C_{\mathrm{HbO_2}}(x,y) + C_{\mathrm{HbR}}(x,y), \tag{3}$$

$$SO_2(x,y) = \frac{C_{\mathrm{HbO_2}}(x,y)}{C_{\mathrm{HbO_2}}(x,y) + C_{\mathrm{HbR}}(x,y)}. \tag{4}$$

Note that HbT here represents the total amount of hemoglobin within the resolution cell. Further compensation for the cumulative effect of hemoglobin and contrast agent absorption along the light paths in the above analysis should provide better accuracy of estimation. In the following $SO_2$ image, the vasculature is first segmented from the background based on the reconstructed HbT distribution; then, its $SO_2$ distribution is computed.

## III. RESULTS

### A. *In Vivo* SPAT Molecular Imaging of Integrin $\alpha_v\beta_3$ in Brain Tumors

Previous reports suggest that integrin $\alpha_v\beta_3$, which is overexpressed in newly formed tumor microvesesels, plays an important role in tumor progression, angiogenesis, and metastasis [39]–[41]. Our *in vivo* molecular imaging strategy targets a U87 glioblastoma tumor with IRDye800-c(KRGDf). The binding of IRDye800-c(KRGDf) to U87 tumor cells was proven in vitro by a binding assay (Fig. 4).

We noninvasively imaged *in vivo* the brains of young adult immunocompromised nude mice (Harlan, Co.) containing intracranial U87 glioblastoma xenografts one week after inoculation of tumor cells. As a negative control, SPAT imaged the mice before the administration of IRDye800-c(KRGDf) and showed no signal from the contrast agent as expected. Twenty hours after the administration of IRDye800-c(KRGDf) through the tail vein, the mice were imaged first by a conventional planar fluorescence imaging system and then by the SPAT system. Then the brain was harvested for validation.

Fig. 3(a) shows a segmented fluorescence image superimposed onto a white-light photograph. Before segmentation, the fluorescence intensity in the tumor focus is about 1.7 times higher than that in the normal brain background. This image verifies the uptake of the IRDye800-c(KRGDf) in the U87 glioblastoma tumor. Fig. 3(b) and (c) shows an *in vivo* SPAT molecular image of IRDye800-c(KRGDf) and a composite SPAT image made by superimposing the segmented molecular image of IRDye800-c(KRGDf) on the structural image of the brain cortex, respectively. The structural image was the SPAT image acquired at 804 nm. It is clearly seen that the contrast agent is mainly accumulated at the tumor focus. Fig. 3(d) shows a photograph of the excised nude mouse brain with the U87 glioblastoma tumor; the tumor focus can be seen on the right hemisphere of the brain. The tumor positions in Fig. 3(c) and (d) agree. Fig. 3(e) shows a microfluorescence image of a frozen brain section acquired postmortem using a fluorescence imaging system (Odyssey; Li-Cor, Inc.). The depth of this section is ~1 mm below the surface of the brain cortex or ~3 mm beneath the scalp surface. This image verifies again the uptake of the molecular probe. Fig. 3(f) shows a photograph of a Thionine-stained section of the excised nude mouse brain, which was sliced from approximately the same depth as the section for Fig. 3(e). This

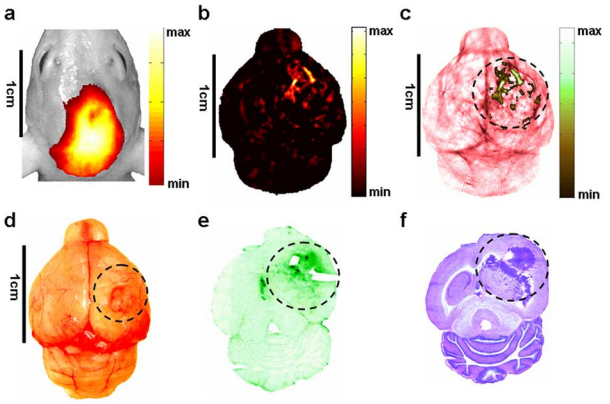


**Fig. 3.** *In vivo molecular imaging of a nude mouse brain with a U87 glioblastoma xenograft by SPAT and validations. (a) Composite of segmented conventional fluorescence image and white-light photograph of the nude mouse head acquired in vivo 20 h after intravenous injection of IRDye800-c(KRGDf). (b) In vivo SPAT molecular image of IRDye800-c(KRGDf). (c) Composite of segmented molecular image of IRDye800-c(KRGDf) and structural image, both acquired in vivo with SPAT. (d) Photograph of the excised nude mouse brain acquired postmortem. (e) Microfluorescence image of a frozen brain section ~1 mm below the brain cortex. (f) Photograph of a Thionine-stained brain section ~1 mm below the brain cortex. The dashed circles indicate the locations of the glioblastoma xenograft.*

histological evaluation further reveals the depth and location of the U87 glioblastoma tumor.

For Fig. 3(c), two ultrasonic transducers with different center frequencies were used to achieve both high spatial resolution for structural imaging and high sensitivity for molecular imaging [31], [32]. A 10-MHz transducer provided the structural image of HbT with a 60-$\mu$m in-plane resolution, whereas a lower-frequency 2.25-MHz transducer provided the molecular image with a 312-$\mu$m in-plane resolution. Both resolutions are significantly better than that in the fluorescence image [Fig. 3(a)].

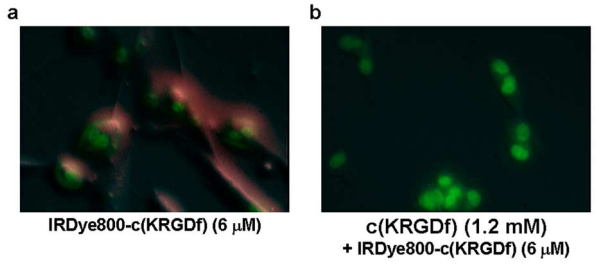


**Fig. 4.** *In vitro binding of IRDye800-c(KRGDf) to U87 tumor cells expressing integrin $\alpha_v\beta_3$. (a) Fluorescence microscopic image of U87 cells incubated with 6 $\mu$M of IRDye800-c(KRGDf) for 3 min. (b) Fluorescence microscopic image of U87 cells incubated with an excess 1.2 mM of c(KRGDf) for 5 min followed by 6 $\mu$M of IRDye800-c(KRGDf) for 3 min. Red: IRDye800-c(KRGDf); green: Sytox green-labeled cell nuclei.*

## B. *In Vivo* SPAT Hypoxia Imaging in Brain Tumor Vasculature

Fig. 5(a) and (b) shows the $SO_2$ and HbT images, respectively, of the nude mouse brain shown in Fig. 3. The tumor focus shows lower $SO_2$ than the surrounding normal tissue, which indicates hypoxic tumor vasculature; it also shows higher HbT, which indicates probable angiogenesis. The hypoxic area in Fig. 5(a) is slightly larger than the uptake area of IRDye800-c(KRGDf) in Fig. 5(b), possibly because hypermetabolism affects the blood supply of not only the tumor proper but also the periphery.

The $SO_2$ and HbT of normal and tumor vasculatures can be quantitatively compared. Fig. 5(c) plots the averages and standard deviations of $SO_2$ in the normal and tumor vasculatures of the brain from three mice; the average $SO_2$ in the tumor vasculature is at least 13% lower than that in the normal vasculature; the $SO_2$ level in the tumor vasculature is more heterogeneous than that in the normal vessels, as indicated by the error bars. The absolute HbT levels cannot be compared among the three mice because they depend on the different conditions of oxygen inhalation and anesthesia. Hence, a relative HbT (rHbT)—defined as the ratio of the local HbT to the mean HbT in the medium fissure of each mouse—is adopted. Fig. 5(d) plots $SO_2$ versus rHbT in the normal and tumor vasculatures of the brain. The normal vessels tend to have a lower rHbT in addition to a higher $SO_2$ and a lower $SO_2$ fluctuation than the tumor vessels.

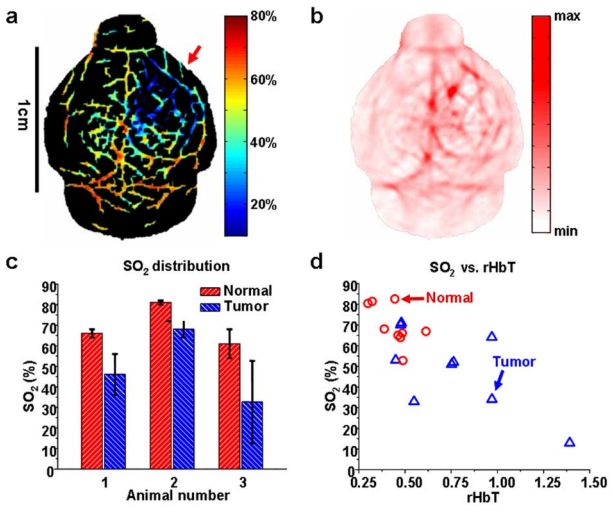


**Fig. 5.** *In vivo functional imaging of a nude mouse brain with a U87 glioblastoma xenograft by SPAT. (a) $SO_2$ image of the nude mouse brain shown in Fig. 3. The red arrow indicates the hypoxic region. (b) HbT image of the same nude mouse brain. (c) Comparison of normal and tumor vasculatures in $SO_2$ from triplicate mice. Three normal and three tumor vessels were chosen from each $SO_2$ image for the calculation. Error bar: one standard deviation. (d) The $SO_2$ versus the relative HbT in normal and tumor vasculatures from the same triplicate mice as in (b).*

## IV. DISCUSSION

The experimental results validated that SPAT can image integrin $\alpha_v\beta_3$ conjugated with optical contrast agent in the nude mouse brain with high spatial resolution on a significant depth scale relative to pure optical imaging (e.g., fluorescence imaging). The imaged inhomogeneous distribution of the $\alpha_v\beta_3$-targeted contrast agent at the tumor focus implies vascular heterogeneities in solid brain tumors. This SPAT-based molecular imaging has the potential to unravel noninvasively neoangiogenesis inside the brain to detect early stage cancer and to assess invasive potential at the molecular level since integrin $\alpha_v\beta_3$, in addition to other factors, is incriminated in facilitating angiogenesis, tumor progression, and metastasis.

Photoacoustic imaging was reported to possess molar sensitivities of ICG in phantoms on the order of nano M [42] to $\mu$M [32]. An *in vivo* sensitivity of $\sim$2 fmol of ICG in a resolution cell in the blood stream was also reported [43]. We demonstrated the imaging of 5-$\mu$M IRDye800-c(KRGDf) in 250-$\mu$m inner diameter plastic tubes covered by a slab of chicken tissue of $\sim$2 mm in thickness with a signal-to-noise ratio of $\sim$26 dB (see Fig. 6). As a result, the sensitivity of our SPAT system to IRDye800-c(KRGDf) is $\sim$5 fmol in a resolution cell. Of course, the sensitivity depends on the SPAT parameters; for example, increasing the incident laser energy density toward the maximum permissible exposure can improve the sensitivity [36]. Fig. 6 also verified the efficacy of SPAT in separating the signal contributions from IRDye800-c(KRGDf) and blood; the efficacy can potentially be improved further by the use of more optical wavelengths at the expense of data acquisition time.

Tumor hypoxia revealed by the functional imaging aspect of SPAT can be correlated with the invasion of the U87 glioblastoma cells revealed by the molecular imaging aspect of SPAT. In a separate rat model demonstrating the etiopathogenesis of hypoxia in intracranial tumor xenografts, we evaluated the expressions of the hypoxia-inducible factor-1$\alpha$ (HIF-1$\alpha$), the vascular endothelial growth factor (VEGF), the vascular endothelial growth factor receptor 2 (VEGFR2), and the matrix metalloproteinases-9 (MMP-9) proteins and the associated mRNA levels [26] in hypoxic brain tumor foci [44]; the levels of these proteins and the associated mRNA in the brain tumor foci were found to be higher than those in normal brain tissues. This model supports the SPAT data that show both hypoxia and up-regulation of proteins in the brain tumor foci.

Higher HbT in addition to lower $SO_2$ in the tumor vasculature is observed, as reported in other studies [45], by SPAT. A tumor requires more blood to meet its up-regulated metabolism, which results in higher HbT. Thus, simultaneous imaging of both HbT and $SO_2$ as well as biomarkers such as integrin $\alpha_v\beta_3$ provide complementary information about tumor biological properties, which can be potentially useful for cell-centered diagnosis, prognosis, and therapies.

The major limitation of our current SPAT system is the scanning speed. Owing to the low laser PRF, slow wavelength changing, and time-consuming mechanical scanning, the current scanning time is about one hour if four wavelengths, 20 times signal averaging, and 120 scanning steps are used. Faster imaging, however, can be achieved by improving these speed-related factors.

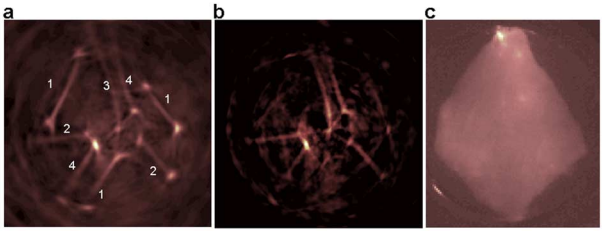


**Fig. 6.** *Imaging of gelatin-embedded 250-$\mu$m inner diameter tubes containing IRDye800-c(KRGDf), oxygenated blood, or a mixture of the two, where the tubes were covered by a slab of chicken tissue of $\sim$2 mm in thickness. (a) Structural image acquired by SPAT at the 804-nm optical wavelength. All tubes were visualized. 1) oxygenated blood, 2) 10 $\mu$M IRDye800-c(KRGDf), 3) 5 $\mu$M IRDye800-c(KRGDf), 4) one-to-one mixture of blood and 10 $\mu$M IRDye800-c(KRGDf). (b) Distribution of IRDye800-c(KRGDf) estimated by SPAT with four wavelengths—764, 784, 804, and 824 nm. In the image, IRDye800-c(KRGDf) was clearly visible while blood was significantly rejected. (c) Fluorescence image of IRDye800-c(KRGDf). The tubes are invisible because conventional fluorescence imaging cannot achieve high spatial resolution in strong scattering tissue.*

## V. CONCLUSIONS

In summary, we have shown that SPAT provides a new paradigm to high-resolution simultaneous molecular and functional imaging of intracranial brain tumors in small animals *in vivo*. In the present SPAT system, the spatial resolution is $\sim$312 $\mu$m for molecular and functional imaging and $\sim$60 $\mu$m for structural imaging. SPAT may be of great importance in the future for monitoring the development of hypoxia in brain tumors and determining the most suitable type and timing of therapy. Further system improvements can potentially shed new light on *in vivo* hemodynamics and biochemical reactions. This paper should prove to be a new impetus for the molecular imaging community to tailor molecular imaging strategies based on optical absorption. SPAT holds promise for noninvasive monitoring of pathological or physiological reactions (e.g., apoptosis) at the cellular and molecular level. In addition, SPAT is applicable to imaging of gene expression [46] or to monitoring of delivery of vectors to specific cells in gene therapy. We anticipate that SPAT will make profound contributions to the molecular imaging in general.

### A. Supplementary Information

*Method:* For the in vitro binding assay of IRDye800-c(KRGDf) to U87 cells expressing integrin $\alpha_v\beta_3$, U87 cells were seeded on cover slips in 24-well plates and incubated

in DMEM/F-12 culture medium (0.5 mL/well) overnight. IRDye800-c(KRGDf) at a concentration of 6 $\mu$M was added to each well for 3 min. The cells were washed twice with phosphate-buffered saline (PBS) and incubated in a solution of Sytox green in 95% ethyl alcohol (1 $\mu$M, Molecular Probes) for 15 min to fix and stain the cell nuclei. The cells were washed again with PBS; then, the cover slips were mounted for microscopic examination. For the blocking test, 1.2 mM of unconjugated c(KRGDf) was added to the culture medium 5 min before the addition of IRDye800-c(KRGDf).

*Results:* As shown in the binding test (a), IRDye800-c(KRGDf) bound to U87 cells. As shown in the blocking test (b), no IRDye800-c(KRGDf) was uptaken because the unlabelled c(KRGDf) preemptively blocked the $\alpha_v\beta_3$ receptors of the U87 cells. ■

## Acknowledgment

The authors are grateful to S. Similache and O. Cracium for their assistance with the veterinary procedures.

## REFERENCES


[1] R. Weissleder and U. Mahmood, "Molecular imaging," *Radiology*, vol. 219, pp. 316–333, 2001.

[2] T. F. Massoud and S. S. Gambhir, "Molecular imaging in living subjects: Seeing fundamental biological processes in a new light," *Genes Develop.*, vol. 17, pp. 545–580, 2003.

[3] R. Weissleder, "Molecular imaging: Exploring the next frontier," *Radiology*, vol. 212, pp. 609–614, 1999.

[4] R. G. Blasberg, "Molecular imaging and cancer," *Mol. Cancer Ther.*, vol. 2, pp. 335–343, 2003.

[5] D. A. Sipkins, D. A. Cheresh, M. R. Kazemi, L. M. Nevin, M. D. Bednarski, and K. C. Li, "Detection of tumor angiogenesis *in vivo* by alphaVbeta3-targeted magnetic resonance imaging," *Nat. Med.*, vol. 4, pp. 623–626, 1998.

[6] D. Neri *et al.*, "Targeting by affinity-matured recombinant antibody fragments of an angiogenesis associated fibronectin isoform," *Nat. Biotechnol.*, vol. 15, pp. 1271–1275, 1997.

[7] V. Brower, "Tumor angiogenesis—New drugs on the block," *Nat. Biotechnol.*, vol. 17, pp. 963–968, 1999.

[8] S. Bredow, M. Lewin, B. Hofmann, E. Marecos, and R. Weissleder, "Imaging of tumour neovasculature by targeting the TGF-beta binding receptor endoglin," *Eur. J. Cancer*, vol. 36, pp. 675–681, 2000.

[9] T. Persigehl, W. Heindel, and C. Bremer, "MR and optical approaches to molecular imaging," *Abdom. Imag.*, vol. 30, pp. 342–354, 2005.

[10] P. M. Winter *et al.*, "Molecular imaging of angiogenesis in nascent Vx-2 rabbit tumors using a novel $\alpha_v\beta_3$-targeted nanoparticle and 1.5 Tesla magnetic resonance imaging," *Cancer Res.*, vol. 63, pp. 5838–5843, 2003.

[11] C. Batya, D. Hagit, M. Gila, H. Alon, and N. Michal, "Ferritin as an endogenous MRI reporter for noninvasive imaging of gene expression in C6 glioma tumors," *Neoplasia*, vol. 7, pp. 109–117, 2005.

[12] S. R. Cherry *et al.*, "MicroPET: A high resolution PET scanner for imaging small animals," *IEEE Trans. Nucl. Sci.*, vol. 44, pp. 1161–1166, 1997.

[13] R. Haubner *et al.*, "Noninvasive imaging of alpha(v)beta3 integrin expression using 18F-labeled RGD-containing glycopeptide and positron emission tomography," *Cancer Res.*, vol. 61, pp. 1781–1785, 2001.

[14] V. Sharma, G. D. Luker, and D. Piwnica-Worms, "Molecular imaging of gene expression and protein function *in vivo* with PET and SPECT," *J. Magn. Res. Imag.*, vol. 16, pp. 336–351, 2002.

[15] P. R. Contag, I. N. Olomu, D. K. Stevenson, and C. H. Contag, "Bioluminescent indicators in living mammals," *Nat. Med.*, vol. 4, pp. 245–247, 1998.

[16] R. Y. Tsien, "The green fluorescent protein," *Ann. Rev. Biochem.*, vol. 67, pp. 509–544, 1998.

[17] D. A. Sipkins *et al.*, "*In vivo* imaging of specialized bone marrow endothelial microdomains for tumour engraftment," *Nature*, vol. 435, pp. 969–973, 2005.

[18] W. Wang *et al.*, "Near-infrared optical imaging of integrin $\alpha v\beta 3$ in human tumor xenografts," *Mol. Imag.*, vol. 3, pp. 343–351, 2004.

[19] V. Ntziachristos, J. Ripoll, L. V. Wang, and R. Weissleder, "Looking and listening to light: The evolution of whole-body photonic imaging," *Nat. Biotechnol.*, vol. 23, pp. 313–320, 2005.

[20] G. M. Lanza and S. A. Wickline, "Targeted ultrasonic contrast agents for molecular imaging and therapy," *Prog. Cardiovasc. Dis.*, vol. 44, pp. 13–31, 2001.

[21] F. F. Jobsis, "Noninvasive, infrared monitoring of cerebral and myocardial oxygen sufficiency and circulatory parameters," *Science*, vol. 198, pp. 1264–1267, 1977.

[22] A. Villringer and B. Chance, "Non-invasive optical spectroscopy and imaging of human brain function," *Trends. Neurosci.*, vol. 20, pp. 435–442, 1997.

[23] C. Menon *et al.*, "An integrated approach to measuring tumor oxygen status using human melanoma xenografts as a model," *Cancer Res.*, vol. 63, pp. 7232–7240, 2003.

[24] A. J. Giaccia, "Hypoxic stress proteins: Survival of the fittest," *Semin. Rad. Oncol.*, vol. 6, pp. 46–58, 1996.

[25] J. M. Brown and A. J. Giaccia, "The unique physiology of solid tumors: Opportunities (and problems) for cancer therapy," *Cancer Res.*, vol. 58, pp. 1408–1416, 1998.

[26] B. Kaur *et al.*, "Hypoxia and the hypoxia-inducible-factor pathway in glioma growth and angiogenesis," *Neuro-Oncology*, vol. 7, pp. 134–153, 2005.

[27] M. Hockel and P. Vaupel, "Tumor hypoxia: Definitions and current clinical, biologic, and molecular aspects," *J. Nat. Cancer Inst.*, vol. 93, pp. 266–276, 2001.

[28] G. J. Diebold and T. Sun, "Generation of ultrasonic waves from a layered photoacoustic source," *Nature*, vol. 355, pp. 806–808, 1992.

[29] X. Wang *et al.*, "Noninvasive laser-induced photoacoustic tomography for structural and functional *in vivo* imaging of the brain," *Nat. Biotechnol.*, vol. 21, pp. 803–806, 2003.

[30] L. V. Wang, "Ultrasound-mediated biophotonic imaging: A review of acousto-optical tomography and photo-acoustic tomography," *Dis. Markers*, vol. 19, pp. 123–138, 2004.

[31] G. Ku, X. Wang, G. Stoica, and L. V. Wang, "Multiple-bandwidth photoacoustic tomography," *Phys. Med. Biol.*, vol. 49, pp. 1329–1338, 2004.

[32] G. Ku and L. V. Wang, "Deeply penetrating photoacoustic tomography in biological tissues enhanced with an optical contrast agent," *Opt. Lett.*, vol. 30, pp. 507–509, 2005.

[33] B. S. Sorg, B. J. Moeller, O. Donovan, Y. Cao, and M. W. Dewhirst, "Hyperspectra imaging of hemoglobin saturation in tumor microvasculature and tumor hypoxia development," *J. Biomed. Opt.*, vol. 10, pp. 044004-1–044004-11, 2005.

[34] S. Lal *et al.*, "An implantable guide-screw system for brain tumor studies in small animals," *J. Neurosurg.*, vol. 92, pp. 326–333, 2000.

[35] U.S. National Institutes of Health, *Guide for the Care and Use of Laboratory Animals*, NIH publication no. 86-23: U.S. Government Printing Office, Washington DC, 1985.

[36] *American National Standard for the Safe Use of Lasers*, ANSI Standard Z136, 2007.

[37] M. Xu, Y. Xu, and L. V. Wang, "Time-domain reconstruction algorithms and numerical simulations for thermoacoustic tomography in various geometries," *IEEE Trans. Biomed. Eng.*, vol. 50, pp. 1086–1099, 2003.

[38] J. Laufer, C. Elwell, D. Delpy, and P. Beard, "*In vitro* measurements of absolute blood oxygen saturation using pulsed near-infrared photoacoustic spectroscopy: Accuracy and resolution," *Phys. Med. Biol.*, vol. 50, pp. 4409–4428, 2005.

[39] P. C. Brooks, R. A. Clark, and D. A. Cheresh, "Requirement of vascular integrin alpha v beta 3 for angiogenesis," *Science*, vol. 264, pp. 569–571, 1994.

[40] B. Felding-Habermann, B. M. Mueller, C. A. Romerdahl, and D. A. Cheresh, "Involvement of integrin alpha V gene expression in human melanoma tumorigenicity," *J. Clin. Invest.*, vol. 89, pp. 2018–2022, 1992.

[41] P. C. Brooks, S. Stromblad, R. Klemke, D. Visscher, F. H. Sarkar, and D. A. Cheresh, "Antiintegrin alpha v beta 3 blocks human breast cancer growth and angiogenesis in human skin," *J. Clin. Invest.*, vol. 96, pp. 1815–1822, 1995.

[42] R. A. Kruger, W. Kiser, D. R. Reinecke, G. A. Kruger, and K. D. Miller, "Thermoacoustic optical molecular imaging of small animals," *Mol. Imag.*, vol. 2, pp. 113–123, 2003.

[43] X. Wang *et al.*, "Non-invasive photoacoustic angiography of animal brains *in vivo* with NIR light and an optical contrast agent," *Opt. Lett.*, vol. 29, pp. 730–732, 2004.

[44] G. F. Lungu, M.-L. Li, X. Xie, L. V. Wang, and G. Stoica, "*In vivo* imaging and characterization of hypoxia-induced neovascularization and tumor invasion," *Int. J. Oncol.*, vol. 30, pp. 45–54, 2007.

[45] D. Grosenick, H. Wabnitz, and K. T. Moesta, "Concentration and oxygen saturation of haemoglobin of 50 breast tumours determined by time-domain optical mammography," *Phys. Med. Biol.*, vol. 49, pp. 1165–1181, 2004.

[46] L. Li, R. J. Zemp, G. Lungu, G. Stoica, and L. V. Wang, "Photoacoustic imaging of lacZ gene expression *in vivo*," *J. Biomed. Opt.*, vol. 12, pp. 020504-1–020504-3, 2007.

## ABOUT THE AUTHORS

**Meng-Lin Li** (Member, IEEE) was born in Tainan, Taiwan, R.O.C., on November 11, 1976. He received the B.S. and Ph.D. degrees in electrical engineering from National Taiwan University, Taiwan, in 1999 and 2004, respectively.

His doctoral work included the investigation of novel ultrasonic adaptive imaging and vector flow estimation methods and the development of a high-frequency small animal imaging system. In 2004, he joined the Optical Imaging Laboratory, Department of Biomedical Engineering, Texas A&M University, as a Postdoctoral Research Associate. In the Optical Imaging Laboratory, his work focused on the development of spectroscopic photoacoustic tomography and microscopy for functional and molecular imaging. In 2006, he returned to Taiwan and joined the Department of Electrical Engineering, National Tsing Hua University, Hsinchu, Taiwan, where he is currently an Assistant Professor. His current research interests include biomedical photoacoustic imaging, ultrasonic imaging, and signal processing.

**Jung-Taek Oh** received the doctoral degree in mechanics from the Korea Advanced Institute of Science and Technology, South Korea.

He is a Senior Engineer with the Telecommunication Center, Samsung Electronics Co., Ltd. His research is primarily focused on two areas: 1) the development of biosensors for biofeedback associated with handheld mobile devices and 2) the development of high-resolution optical tomography system for functional image and diagnosis.

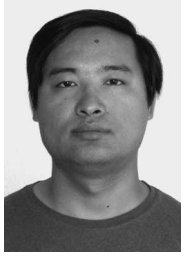

**Xueyi Xie** received the undergraduate degree from TsingDao University, China, and the master's degree from North Texas State University, Denton. He is currently pursuing the Ph.D. degree in the Department of Pathobiology, Texas A&M University, College Station.

His research is primarily focused on three areas: 1) malignant tumor pathobiology, 2) biomedical imaging, and 3) rat brain neuron degeneration pathology.

**Geng Ku** received the B.S. and M.S. degrees from Huazhong University of Science and Technology, China, and the Ph.D. degree in biomedical engineering from Texas A&M University, College Station.

He is a Research Faculty Member with the Department of Biomedical Engineering, Washington University in St. Louis. His research is primarily focused on laser-based photoacoustic tomography and microwave-based thermoacoustic tomography.

**Wei Wang** received the undergraduate degree from Beijing Chemical Engineering Institute, Beijing, China, and the doctoral degree in chemistry from the University of Stuttgart, Stuttgart, Germany.

She is an Assistant Professor in the Department of Radiology, Baylor College of Medicine, Waco, TX. Her research is focused on development of targeted imaging probes for noninvasive, single- or multimodality imaging in various applications.

**Chun Li** received the undergraduate degree from Peking University, Beijing, China, and the doctoral degree in chemistry from Rutgers—The State University, New Brunswick, NJ.

He is currently a Professor and Chemist with the Department of Experimental Diagnostic Imaging, University of Texas M. D. Anderson Cancer Center. Research in his laboratory is primarily focused on two areas: 1) the development of targeted imaging probes for noninvasive characterization of molecular events associated with tumor progression and regression and 2) the development of novel drug-delivery systems for selective delivery of diagnostic and therapeutic agents.

**Gina Lungu** received the bachelor's degree in biochemistry from the University of Bucharest, Romania, and the master of science degree in biology from Texas Woman's University, Denton.

She is an Assistant Research Scientist with the Department of Pathobiology, College of Veterinary Medicine, Texas A&M University, College Station. Her research is primarily focused on the 1) mechanisms of breast cancer brain metastasis in a rat model and 2) mechanisms of retroviral-induced neurodegeneration.

**George Stoica** received the M.Sc. degree from The Ohio State University, Columbus, and the Ph.D. degree in experimental pathology from Michigan State University, East Lansing.

He is a Professor in the Department of Veterinary Pathobiology, College of Veterinary Medicine, Texas A&M University, College Station. His major research interest is in developing animal models for human diseases such as AIDS-related neurodegeneration, ataxia telengiectasia, Alzheimer's and Parkinson's diseases, and neoplasias. He is also involved in developing new technologies with clinical application in animal models such as photoacoustic tomography, optical coherence tomography, and novel drug-delivery systems for selective delivery of diagnostic and therapeutic agents.

**Lihong V. Wang** (Fellow, IEEE) received the Ph.D. degree from Rice University, Houston, TX.

He currently holds the Gene K. Beare Distinguished Professorship in the Department of Biomedical Engineering, Washington University in St. Louis. He has published two books and 130 articles in peer-reviewed journals, such as *Nature Biotechnology, Nature Protocols, Physical Review Letters, Physical Review, Optics Letters*, and IEEE TRANSACTIONS. He has delivered 130 plenary, keynote, and invited talks. He is a member of the editorial boards of two journals. He chairs the scientific advisory board of a company. His group invented frequency-swept ultrasound-modulated optical tomography, dark-field confocal photoacoustic microscopy, exact reconstruction algorithms for photoacoustic or thermoacoustic computed tomography, Mueller-matrix optical coherence tomography, and oblique-incidence reflectometry. His Monte Carlo model of photon transport in scattering media has been used worldwide. He is Chair of the International Biomedical Optics Society.

Prof. Wang is a Fellow of the American Institute for Medical and Biological Engineering, Optical Society of America, and Society of Photo-Optical Instrumentation Engineers.